# **Deep Optimal Transport on SPD Manifolds for Domain Adaptation**

#### Ce Ju and Cuntai Guan

S-Lab, Nanyang Technological University {juce0001,ctguan}@ntu.edu.sg

#### **Abstract**

The domain adaption (DA) problem on symmetric positive definite (SPD) manifolds has raised interest in the machine learning community because of the growing potential for the SPD-matrix representations across many non-stationary applicable scenarios. This paper generalizes the joint distribution adaption (JDA) to align the source and target domains on SPD manifolds and proposes a deep network architecture, Deep Optimal Transport (DOT), using the generalized JDA and the existing deep network architectures on SPD manifolds. The specific architecture in DOT enables it to learn an approximate optimal transport (OT) solution to the DA problems on SPD manifolds. In the experiments, DOT exhibits a 2.32% and 2.92% increase on the average accuracy in two highly non-stationary cross-session scenarios in brain-computer interfaces (BCIs), respectively. The visualizational results of the source and target domains before and after the transformation also demonstrate the validity of DOT.

#### 1 INTRODUCTION

For real-world applications, a signal or an image in the online testing set is often not a realization of the same process that generates it for the calibration set. For instance, the nonstationarity change of EEG signals, such as the bias and covariate shifts, happens from session to session or from calibration to feedback within a session. It is known as the DA problem in the machine learning community (Ben-David et al., 2007), which has attracted much attention during the past ten years. The principal idea of tackling the DA problem is to improve the classifier's performance deployed on the target domain using labeled data of a source domain. Typically, there is very few or even no labeled data on the target domain. Despite many existing pieces of literature against the DA problem, for example, JDA (Long et al., 2013), more recently, OT has been exploited and paved a new path to align the source and target domains. For example, Courty et al. (2016, 2017) extend regularized OT algorithms to a framework for the (semi)-supervised DA problem so that the classifier can learn from the labeled source data and deploy on the target data, and propose a solution to recover the estimated target with a theoretical guaranty for convergence. Further, Yair *et al.* (2019) generalize their framework on SPD manifolds and demonstrate OT is the optimal solution to the DA problem in a well-defined situation using the polar factorization theorem on manifolds (McCann, 2001).

The most fruitful part of their work is actually to jump out at addressing a critical problem of generalizing DA on the space of SPD matrices. Because SPD matrices play an increasing role in many disciplines in science and engineering as a powerful data representation, such as diffusion tensor imaging, computer vision, radar signal processing, and braincomputer interface. (Minh and Murino, 2017) To illustrate, a representation of 2D images in the covariance matrix is SPD. It has recently emerged in computer vision because of its compactness, robustness to noise, and flexible scalability in many computer vision tasks. As another example, a representation of electroencephalogram (EEG) signals in spatial covariance matrix is also SPD and has been studied in common spatial patterns (Koles et al., 1990) in BCIs for 20 years until it was revealed as an SPD matrix by Barachant et al. (2011) for the first time and generalized in a framework of SPD manifolds. The SPD manifold is the space of SPD matrices equipped with a given Riemannian metric. In their works, the geodesic distance on SPD manifolds encoded as the high-level feature for EEG classification has exhibited to work well. As a consequence, Ju et al. (2020) exploit the low-level features in spatial covariance matrices of EEG signals for classification using a Riemannian-based network architecture SPDNet (Huang and Van Gool, 2017) and transfer the knowledge from the source domain to a common latent space with an empirical Maximum Mean Discrepancy (MMD) approach (Huang et al., 2006).

The aim of the present study is therefore multifold: 1): The JDA approach is generalized on SPD manifolds by minimizing the geodesic distance between the empirical centroids of the source and target domains on SDP manifolds. 2): We propose a novel deep network framework DOT using the generalized JDA approach and the architecture of SPDNet against the DA problem on SPD manifolds. We exhibit that the weights in the BiMap layer of DOT are an approximate OT solution to the DA problem on SPD manifolds. 3): Due to the highly non-stationarity across sessions (a.k.a., the inter-session variability) of neural signals, we testify DOT on the cross-session scenario of two well-known EEG-based BCI datasets and visualize the statistical distributions of the source and target domains before and after the transformation.

## 2 PRELIMINARY

#### 2.1 Notations

 $Gl(n) := \{S \in \mathbb{R}^{n \times n} : \det S \neq 0\}$  is the general linear group.  $\mathcal{S}^n := \{S \in \mathbb{R}^{n \times n} : S = S^\top\}$  is the space of  $n \times n$  real symmetric matrices, and  $\mathcal{S}^n_{++} := \{S \in \mathcal{S}^n : x^\top Sx > 0, \forall x \in \mathbb{R}^n/\{0\}\}$  is the space of  $n \times n$  real SPD matrices. The Frobenius inner product and Frobenius norm on  $m \times n$  matrices A and B are defined as  $\langle A, B \rangle_{\mathcal{F}} := \operatorname{Tr}(A^\top B)$  and  $\|A\|^2_{\mathcal{F}} := \langle A, A \rangle_{\mathcal{F}}$  respectively.

#### 2.2 SPD Manifolds with the Log-Euclidean Metric

The space of  $n\times n$  real SPD matrices  $\mathcal{S}^n_{++}$  is given a commutative Lie group structure if equipped with a logarithmic multiplication  $\odot$  such that  $S_1\odot S_2:=\exp\left(\log(S_1)+\log(S_2)\right)$  for  $S_1,S_2\in\mathcal{S}^n_{++}$ , where  $\exp$  and  $\log$  are matrix exponential and logarithm respectively. (Arsigny et al., 2005, Def. 3) A Log-Euclidean metric is a (Lie-group) bi-invariant metric defined on  $\mathcal{S}^n_{++}$  such that the left- and right-multiplication by any  $S\in\mathcal{S}^n_{++}$  are isometries. The Riemannian manifold  $\mathcal{S}^n_{++}$  with Log-Euclidean metric is denoted as  $(\mathcal{S}^n_{++},$  LEM) in this paper. The Log-Euclidean  $geodesic^1$   $\gamma(t):[0,1]\longmapsto\mathcal{S}^n_{++}$  between any two SPD matrices  $S_1$  and  $S_2$  of  $(\mathcal{S}^n_{++},$  LEM) such that  $\gamma(0):=S_1,$   $\gamma(1):=S_2$  and  $\gamma(t):=\exp\left((1-t)\cdot\log S_1+t\cdot\log S_2\right)$  with the arc-length of geodesic given in (Arsigny et al., 2005, Cor. 4) as follows,

$$\mathcal{L}_{LEM}(\gamma) = ||\log(S_1) - \log(S_2)||_{\mathcal{F}}. \tag{1}$$

The Log-Euclidean Fréchet mean  $Bar_w(\mathcal{B})$  of a batch  $\mathcal{B}$  of SPD matrices  $\{S_i\}_{i=1}^{|\mathcal{B}|} \in (\mathcal{S}^n_{++}, \text{LEM})$  is given in (Arsigny et al., 2005, Thm. 6) as follows,

$$Bar_w(\mathcal{B}) := \exp\left(\frac{1}{|\mathcal{B}|} \cdot \sum_i w_i \cdot \log(S_i)\right).$$
 (2)

For a more in-depth material for Riemannian geometry of SPD matrices, we refer the readers to (Petersen *et al.*, 2006; Bhatia, 2009; Minh and Murino, 2017).

# 2.3 Joint Distribution Adaptation

In a cross-domain problem, the source data distribution is usually not identical to the target data distribution. Hence, a critical computational issue of domain adaptation is to align the data distributions across source domain  $\mathcal{D}_S$  and target domain  $\mathcal{D}_T$ . Joint distribution adaptation (Long *et al.*, 2013) is proposed to jointly adopt both marginal and conditional distributions between domains, whereas label information is not required in the target domain. Formally, given a labeled source domain  $\mathcal{D}_S = \{x_s, y_s\}_{s=1}^n$  and an unlabeled target domain  $\mathcal{D}_T = \{x_t\}_{t=1}^m$ , assume the feature space  $X_S = X_T$  and label space  $Y_S = Y_T$ , whereas the marginal distributions  $P_S(X_S) \neq P_T(X_T)$  and conditional distribution  $Q_S(Y_S|X_S) \neq Q_T(Y_T|X_T)$ . The goal of JDA is to build a prediction model  $f: x_s \in \mathcal{D}_S \longmapsto y_t \in \mathcal{D}_T$  explicitly reducing the distribution differences between both marginal distribution  $P_S(X_S)$  and  $P_T(X_T)$ , and conditional distributions  $Q_S(Y_S|X_S)$  and  $Q_T(Y_T|X_T)$ .

#### 2.4 SPDNet

SPDNet (Huang and Van Gool, 2017) is a deep learning architecture fed with SPD matrices that preserves the SPD structure across layers during non-linearly learning. Analogous to convolutional neural networks, the basic layers in SPDNet are designed concerning SPD structure, including the following layers:

- BiMap: This layer transforms the covariance matrix S using bi-map operator W·S·W<sup>T</sup>. Transformation matrix W is required to be full row rank.
- Riemannian Batch Normalization (BN): This layer enables the batch normalization operator to work on Riemannian manifolds, attributed to (Cho and Lee, 2017; Brooks *et al.*, 2019).
- ReEig: This layer is analogous to ReLU in classical deep neural networks that introduces the non-linearity on SPD manifolds using  $U \cdot \max{(\epsilon I, \Sigma)} \cdot U^T$ , where  $S = U \cdot \Sigma \cdot U^T$ , and  $\epsilon$  is a rectification threshold and I is an identity matrix.
- LOG: This layer is to map elements on SPD manifolds on its tangent space using U · log (Σ) · U<sup>T</sup>, where S = U · Σ · U<sup>T</sup>.

### 2.5 Optimal Transport on Riemannian Manifolds

Let  $(\mathcal{M},g)$  be a connected, compact, and  $C^3$  smooth Riemannian manifold without boundary, equipped with a Riemannian distance d(x,y). Optimal transport on  $(\mathcal{M},g)$  in Monge's formulation looks for a (Borel) measurable map  $T:\mathcal{M}\mapsto\mathcal{M}$  to push a prior probability measure  $\mu\in\mathcal{P}(\mathcal{M})$  to a target measure  $\nu\in\mathcal{P}(\mathcal{M})$ , i.e.,  $\nu(A)=\mu(T^{-1}(A))$  for all measurable  $A\subset M$ , and to minimize the transport cost as follows,

$$C(s) := \int_{M} c(x, T(x)) d\mu(x),$$

where  $c:\mathcal{M}\times\mathcal{M}\mapsto\mathbb{R}$  is a given cost function. Notably, in Kantarovich's formulation, measurable map T is a bi-measure on  $\mathcal{M}\times\mathcal{M}$  called a transport plan. McCann (2001) proves that given any compactly supported measures  $\mu,\nu\in\mathcal{P}(\mathcal{M})$ , if  $\mu$  is absolutely continuous w.r.t the volume measure, there exists unique transport map  $T(x)=\exp_x[-\nabla\psi(x)]$  w.r.t cost  $c(x,y)=d(x,y)^2/2$ , where  $\psi:\mathcal{M}\mapsto\mathbb{R}$  is a c-concave function (a.k.a. Kantorovich potential), exp is the exponential map on Riemannian manifolds. Kim and Pass (2015) generalize McCann's theorem to multi-marginal scenarios on Riemannian manifolds with the cost function of average distance squared between barycenters. For more thorough background and applications in the machine learning society on optimal transport, we refer the readers to (Villani, 2009; Kolouri  $et\ al.$ , 2017)

#### 3 PROPOSED METHODOLOGY

In the proposed methodology, we will first generalize JDA on  $(S_{++}^n, \text{LEM})$  to be the cost function in optimal transport. Technically, both marginal distribution adaptation (MDA) and conditional distribution adaptation (CDA) in JDA are generalized on SPD manifolds respectively, as illustrated in Fig. 1

<sup>&</sup>lt;sup>1</sup> Formal definition of geodesic on Riemannian manifolds (M,g) with respect to the Levi-Civita connection  $\nabla$  is defined as a curve  $\gamma(t)$  such that  $\nabla_{\dot{\gamma}}\dot{\gamma}=0$ .

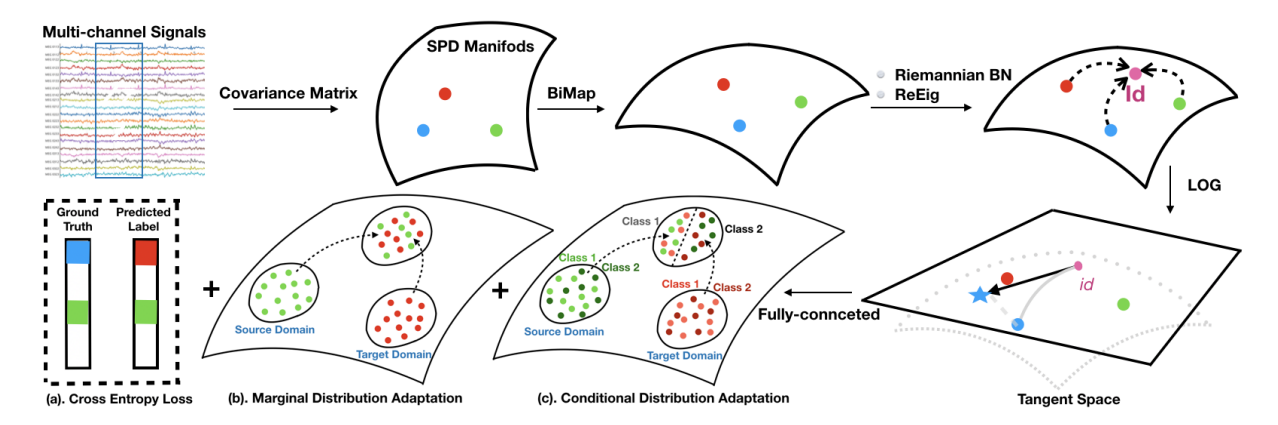


Figure 1: Illustration of the Architecture of Deep Optimal Transport: Data (i.e., multi-channel signals) is first transformed as covariance matrices S on SPD manifolds using a sliding window, then processed through the BiMap, Riemannian BN, ReEig, and LOG layers onto tangent space of SPD manifolds. The loss function takes into account the cross-entropy, MDA loss, and CDA loss on  $(S_{++}^n, \text{LEM})$ . Notably, (b) and (c) illustrate the cases in which the dimension of the outcomes on tangent space is the same as one of the covariance matrices.

(b) and (c). After that, we will propose a novel deep transfer learning approach DOT using the generalized JDA on  $(S_{++}^n, LEM)$ . The network architecture of ODA refers to Fig. 1.

# 3.1 Joint Distribution Adaptation on $(S_{++}^n, LEM)$ Marginal Distribution Adaptation (MDA)

The aim of MDA is to adapt marginal distributions  $P_S(X_S)$  and  $P_T(X_T)$  on  $(\mathcal{S}^n_{++}, \text{LEM})$ . We measure the statistical difference between them using the Log-Euclidean distance in Equ. 1 between Log-Euclidean Fréchet means of each batch of source and target samples  $\mathcal{B}_S$  and  $\mathcal{B}_T$ , i.e.,

$$\mathcal{L}_{LEM}(\gamma) = ||\log \left(Bar_w(\mathcal{B}_S)\right) - \log \left(Bar_w(\mathcal{B}_T)\right)||_{\mathcal{F}}^2,$$

where Log-Euclidean geodesic  $\gamma(t):[0,1] \longmapsto \mathcal{S}_{++}^n$  such that  $\gamma(0):=Bar_w(\mathcal{B}_S)$  and  $\gamma(1):=Bar_w(\mathcal{B}_T)$ . Impressively, plug in Equ. 2 and let  $w=\{1,\cdots,1\}$ ,  $\mathcal{L}_{LEM}(\gamma)$  has an explicit and simple expression as follows,

$$\left\| \frac{1}{|\mathcal{B}_S|} \cdot \sum_{S_i \in \mathcal{B}_S} \log\left(S_i\right) - \frac{1}{|\mathcal{B}_T|} \cdot \sum_{S_j \in \mathcal{B}_T} \log\left(S_j\right) \right\|_{\mathcal{F}}^2, \quad (3)$$

where  $\log(S_i)$   $(S_i \in \mathcal{B}_S)$  and  $\log(S_j)$   $(S_j \in \mathcal{B}_T)$  are the outputs after the LOG Layer.

#### **Conditional Distribution Adaptation (CDA)**

The aim of CDA is to adapt condition distributions  $Q_S(y_S|x_S)$  and  $Q_T(y_T|x_T)$  on  $(\mathcal{S}^n_{++}, \text{LEM})$ . We follow the approach in (Long et al., 2013) in which the authors take into account class-conditional distribution Q(X|Y) instead of posterior probability Q(Y|X), and propose to employ pseudo labels  $\hat{y}$  against the unsupervised setting. To measure the statistical difference between  $Q_S(y_S|x_S)$  and  $Q_T(y_T|x_T)$ , we keep on going to use the Log-Euclidean distance between the Log-Euclidean Fréchet means of each batch of source samples  $S^l := \{x_S \in S | \hat{y}_S = l \}$  and target samples  $T^l := \{x_T \in T | \hat{y}_T = l \}$  within the class  $l \ (1 \le l \le L)$ , i.e.,

$$\mathcal{L}_{LEM}(\gamma^l) = ||\log\left(Bar_w(\mathcal{B}_{S^l})\right) - \log\left(Bar_w(\mathcal{B}_{T^l})\right)||_{\mathcal{F}}^2,$$

where Log-Euclidean geodesic  $\gamma^l(t):[0,1] \longmapsto \mathcal{S}^n_{++}$  such that  $\gamma^l(0):=Bar_w(\mathcal{B}_{S^l})$  and  $\gamma^l(1):=Bar_w(\mathcal{B}_{T^l})$ . Using the same argument as Equ. 3, the distances are explicitly expressed as follows,

$$\left\| \frac{1}{|\mathcal{B}_{S^l}|} \cdot \sum_{S_i^l \in \mathcal{B}_{S^l}} \log\left(S_i^l\right) - \frac{1}{|\mathcal{B}_{T^l}|} \cdot \sum_{S_j^l \in \mathcal{B}_{T^l}} \log\left(S_j^l\right) \right\|_{\mathcal{F}}^2, \tag{4}$$

where  $\log{(S_i^l)}$   $(S_i \in \mathcal{B}_{S^l})$  and  $\log{(S_j^l)}$   $(S_j \in \mathcal{B}_{T^l})$  are the outputs after the LOG Layer.

**Note:** 1). To the best of our knowledge, this is the first time to leverage the JDA approach on SPD manifolds. 2). There are many alternative Riemannian metrics on  $S_{++}^n$ , i.e. affine invariant Riemannian metric (AIRM) (Pennec et al., 2006). Existing literatures (Chen et al., 2020) has broadly discussed the learning performance under each metric. However, LEM is the best choice in our case because, for example, the Fréchet mean of  $(S_{++}^n, AIRM)$  can only be calculated in an iteration method which is not convenient put as a loss function in the deep neural networks. Cautious discussions of different Riemannian metrics on SPD manifolds refer to Appendix C. 3). Equ. 3 and 4 have a two-fold interpretation w.r.t. the methodology in domain adaptation. On one hand, it is an empirical MMD approach in which the feature map  $\varphi(x) := \log(x)$  and reproducing kernel Hilbert space  $\mathcal{H} := \mathbb{R}^d$  with *Frobenius* norm, where d is the output dimension. On the other hand, because each S either from  $\mathcal{B}_S$  or  $\mathcal{B}_T$  is a spatial covariance matrix, it is a correlation alignment (CORAL) approach (Sun and Saenko, 2016; Sun et al., 2017) in which the second-order statistics of the source and target data distributions is aligned to minimize the drift between statistical distributions.

### 3.2 Deep Optimal Transport on SPD Manifolds

In this section, we propose a novel deep transfer learning approach *Deep Optimal Transport* (DOT) whose network architecture consists of existing architecture in SPDNet, which has been introduced in Section 2.4. The loss function  $\mathcal{L}$  of DOT is made of the cross-entropy (CE) loss  $\mathcal{L}_C$  and the leveraged JDA on  $(\mathcal{S}_{++}^n, \text{LEM})$  termed as the MDA loss  $\mathcal{L}_{MDA}$ 

and the CDA loss  $\mathcal{L}_{CDA}$ , i.e.,

$$\mathcal{L} := \alpha_1 \cdot \mathcal{L}_C + \alpha_2 \cdot \mathcal{L}_{MDA}^2 + \alpha_3 \cdot \mathcal{L}_{CDA}^2, \tag{5}$$

where  $\alpha_1, \alpha_2, \alpha_3 \geq 0$ ,  $\mathcal{L}_{MDA} := \mathcal{L}_{LEM}(\gamma)$ , and  $\mathcal{L}_{CDA} := \sum_{l=1}^{L} \mathcal{L}_{LEM}(\eta^l)$  with Log-Euclidean geodesic  $\gamma(t), \eta^i(t) := [0,1] \longmapsto \mathcal{S}_{++}^n$  such that  $\gamma(0) := Bar_w(\mathcal{B}_S), \ \gamma(1) := Bar_w(\mathcal{B}_T)$ , and  $\eta^l(0) := Bar_w(\mathcal{B}_{S^l}), \ \eta^l(0) := Bar_w(\mathcal{B}_{T^l})$  for 1 < l < L.

The architecture of DOT is so-called *optimal transport* because the BiMap layer in DOT provides a data-driven tool to solve the OT problem on SPD manifolds. Technically, attributed to the Brenier-McCann's polar factorization theorem on Riemannian manifolds, Yair *et al.* (2019) show that bi-map function  $W \cdot S \cdot W^T$  is the transport map to the OT problem on SPD manifolds with the cost function of Euclidean squared distance. This enables the BiMap layer in DOT directly to learn the transformation matrix W in a data-driven manner and to be an *optimal transport* on SPD manifold between the source and target marginal/conditional distributions. It is worth mentioning that the cross-entropy component  $\mathcal{L}_C$  penalizes DOT in a trade-off between the high classification performance and the optimality of transportation.

**Note:** 1). The MDA and CDA losses in Equ. 5 are required to be squared distance according to the theoretical results of optimal transport on Riemannian manifolds (McCann, 2001). 2). Attributed to theoretical results of optimal transport on Riemannian manifolds in the multi-marginal scenario (Kim and Pass, 2015), the loss function of Equ. 5 will be modified as the multi-JDAs between each pair of source and target domains on  $(S_{++}^n$ , LEM) as follows,

$$\mathcal{L} := \alpha_1 \cdot \mathcal{L}_C + \sum_i \left( \alpha_2^i \cdot \mathcal{L}_{MDA}^2 + \alpha_3^i \cdot \mathcal{L}_{CDA}^2 \right).$$

3). For an adaptive version of the loss function, one can pre-set the weights  $\alpha_1, \alpha_2$ , and  $\alpha_3$  using adaptive importance weighted tricks according to the training and test distributions, refer to (Sugiyama *et al.*, 2007; Li *et al.*, 2010). 4). In the unsupervised domain adaption, CDA in the loss function requires pseudo labels for the test set predicted by a baseline algorithm. 5). In the experiments, we use  $DOT(\alpha_1, \alpha_2, \alpha_3)$  to represent DOT architecture with weights in the loss function  $\alpha_1, \alpha_2$ , and  $\alpha_3$ .

#### 4 EXPERIMENTS

#### 4.1 Evaluation Dataset

Cross-session motor imagery (MI) classification is a challenge that has been not well addressed so far. Therefore, in this study, we use the MI scenario to evaluate the proposed approach on the largest BCI dataset for 2-class motor imagery, MI-KU (Lee *et al.*, 2019), as well as the most commonly used benchmarking BCI dataset, BCIC-IV-2a (Brunner *et al.*, 2008).

#### **Korea University Dataset (MI-KU)**

In the MI-KU dataset, 54 subjects performed a binary class MI task. Their EEG signals were recorded with a sampling rate of 1,000 Hz and collected with 62 Ag/AgCl electrodes in which 20 electrodes in the motor cortex region were selected (FC-5/3/1/2/4/6, C-5/3/1/z/2/4/5, and CP-5/3/1/z/2/4/6) for our

evaluation of each classifier. The continuous EEG data were segmented from 1 to 3.5 s w.r.t stimulus onset.

#### BCI Competition IV 2a (BCIC-IV-2a)

BCIC-IV-2a is a cue-based BCI paradigm with the four-class MI-EEG motor imagery task including left hand, right hand, feet, and tongue recorded in 22 Ag/AgCl EEG electrodes and three monopolar EOG channels with 250 Hz sampling rate from 9 subjects. The signal is bandpass-filtered between 0.5 and 100 Hz (with the 50 Hz notch filter enabled). The BCIC-IV-2a dataset has the training session (T), and the evaluation session (E) recorded on different days. In either T session or E session, each subject performed six runs of 12 cue-based trials for each of the four classes, yielding a total of 288 (=  $6 \times 12 \times 4$ ) trials per subject. The continuous EEG data were segmented from 0.5 to 4.5 s w.r.t stimulus onset.

## 4.2 Experimental Settings

The experimental settings for unsupervised domain adaptation on two evaluated datasets are stated as follows, illustrated in 2: 1). For the MI-KU dataset, Session 1 is for training. The first half of Session 2 is for validation, and the second half is for testing. We adopt early stopping in the validation; 2). For the BCIC-IV-2a dataset, Session 1 is for training, and Session 2 is for testing. There is no validation set in this case, and thus we set a maximum epoch value, for example, 500 for stopping in practice.

**Note:** 1). The pre-set number of epochs 500 is enough for DOT to converge on BCIC-IV-2a. 2). We require the knowledge is always transferred from Session 1 (source domain) to Session 2 (target domain), i.e.,  $S1 \rightarrow S2$  on each dataset because of the effects of the learning process and memory mechanism in neurophysiology.

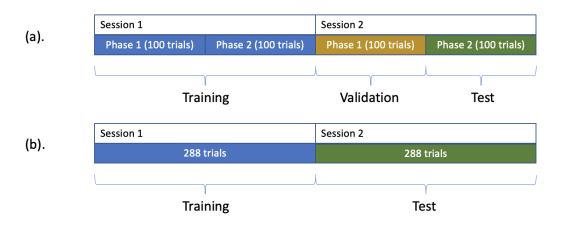


Figure 2: Illustrations for experimental settings of unsupervised domain adaptation on two datasets: (a). MI-KU; (b). BCIC-IV-2a.

#### 4.3 Evaluated Baselines

In this section, we introduce three categories of baselines for the evaluation. Since most machine learning approaches cannot be directly used in the domain of BCIs, we select several BCI-specific algorithms as baselines as follows,

 Covariance Approach: The covariance approach extract features from spatial covariance matrices derived from EEG signals and uses machine learning classifiers for the classification. Three classifiers filters, such as bank common spatial pattern (FBCSP) (Ang et al., 2008), minimum distance to Riemannian mean (MDM), and tangent space mapping (TSM) (Barachant et al., 2011), are selected for the evaluation. FBCSP employs the CSP method on each sub-bands of EEG signals to acquire subband scores and then deploy the classification algorithms on selected features. The other two Riemannian-based approaches, MDM and TSM, employ the geodesic distance on SPD manifolds or its tangent space for the classification.

- 2. Transfer Learning Approach: The transfer learning approach is a broad set of algorithms in machine learning. In our evaluation, Riemannian Procrustes Analysis (RPA) (Rodrigues et al., 2018) is the only selected baseline because it is a transfer learning approach using the geometric transformations (translation, scaling, and rotation) specifically in BCIs. After the geometric transformations, we use MDM as the classifier for the classification. Two subprocesses in RPA, such as RCT and ROT, are independently plotted in the visualization. RCT is a step to recentering the centroids of data to the identity. ROT is the step after RCT to link the centroids of each dataset along the geodesics on manifolds (a.k.a. parallel transport).
- 3. Deep Learning Approach: The deep learning methodology brings the modern classifier for the BCI classification in which the convolution neural networks are used to capture the spatial-frequency patterns and temporal dynamics. Two typical approaches eegNet (Lawhern et al., 2018) and ConvNet (Schirrmeister et al., 2017) are selected in the evaluation. In our experiments, we adopt their specific configurations in the architecture shallow ConvNet and eegNet-4,2, where 4 is the number of temporal filters, and 2 is the number of spatial filters per temporal filter.

#### 4.4 Technique of Filter Banks

For the EEG signals, a widely used technique for data processing is the filter bank approach proposed in (Ang et al., 2008). In the implementation of DOT on SPD manifolds, we adopt this technique in the architecture for data processing that a bank of band-pass filters (i.e.,  $4 \sim 8$  Hz,  $8 \sim 12$  Hz, ...,  $36 \sim 40$  Hz.) is used to decompose the raw oscillatory signals into multiple frequency passbands with the causal Chebyshev Type II filter. DOT will be fed with the 9-channel filtered signals. Remember that we need to map the input of each channel independently to the tangent space across layers and concatenate them on the tangent space before the fully-connected layer.

### 5 Main Result

In this section, we will investigate the average accuracies & standard deviations and the change of Riemannian distances of the proposed approach. In addition, we will visualize the statistical distribution before and after the transformation.

#### **5.1** Average Accuracy

Typically, the performance of BCI classifiers varies widely in data preparation such as the length of EEG segments and electrode placements. Therefore, there is one algorithm FBCSP that is regarded as the most stable baseline in most cases. In our experiments, FBCSP achieves 59.67% and 55.71% on MI-KU and BCIC-IV-2a, respectively, in Table 1. The other

covariance methods, TSM and MDM, perform much worse than FBCSP on both datasets. The three deep learning approaches, shallow ConvNet, eegNet-4,2, and SPDNet, slightly beat FBCSP on MI-KU but around 10% less than the average accuracy of FBCSP. Particularly, since DOT(1, 0, 0) adopts the technique of filter banks, it gains 2.70% and 24.66% increases on two datasets, respectively, compared with SPDNet, whose architecture and loss function is the same as DOT(1,0,0).

Table 1: Average accuracies and standards in the subject-specific analysis of **MI-KU** (54 Subjects in Total) and **BCIC-IV-2a** (9 Subjects in Total). The best-performing number for each analysis is highlighted in boldface. The triple  $(\alpha_1, \alpha_2, \alpha_3)$  after DOT is a portfolio of weights in the loss function of DOT. The methods with \* are the transfer learning approaches training with the labeled training dataset and the unlabeled test dataset.

	$\begin{array}{c} \text{MI-KU} \\ (S1 \rightarrow S2) \end{array}$	BCIC-IV-2a $(T \to E)$
Method	Acc.(Std.) %	Acc.(Std.) %
FBCSP	59.67 (14.32)	55.71 (13.24)
TSM	51.65 (6.11)	39.62 (9.39)
MDM	52.33 (6.74)	40.66 (13.80)
RPA*	54.56 (8.87)	43.79 (11.86)
shallow ConvNet	60.81 (11.32)	41.55 (8.09)
eegNet-4,2	63.26 (11.02)	48.23 (10.52)
SPDNet	60.41 (12.13)	41.59 (10.54)
DOT(1, 0, 0)	63.11 (13.83)	66.25 (14.25)
$DOT(1, 1, 0)^*$	64.24 (13.83)	66.63 (13.23)
$DOT(1, 0, 1)^*$	<b>65.43</b> (13.52)	65.62 (11.71)
$DOT(1, 1, 1)^*$	64.17 (13.83)	<b>69.17</b> (11.93)

In the UDA setting, RPA increases 2.23% and 3.13% upon average accuracies of MDM on two datasets respectively attributed to the additional information from the unlabeled test dataset, refer to Table 2. It exhibits the baseline effects of the primary transportation of statistical distributions such as re-centering and parallel transport on two datasets. Our proposed DOT approach with the CE loss and either the MDA loss, the CDA loss, or the both always surpasses the one only with the CE loss by  $1\%\sim3\%$ . The results demonstrate that the generalized JDA on SPD manifolds is as effective as the optimal transport in RPA for EEG signals. Note that the increase depends on many dataset-specific factors, such as the statistical distribution of datasets and the quality of signals. Additionally, there are cases that DOT loses accuracy with an inappropriate weight ratio in the loss function.

**Note**: Although the improvements of algorithms are around 3% in each dataset, they are effective approaches in the domain of BCIs due to a phenomenon of BCI illiteracy, refer to Section 6.

#### **5.2** Riemannian Distance

This subsection plots average Riemannian distances between source and target domains on two datasets. As the meaning of the MDA and CDA losses, We use them to measure such distances as their original meaning. In Fig. 3, the curves of the MDA and CDA losses go down steadily towards stability.

Table 2: Average accuracy increase (acc. inc.) for the UDA setting on **MI-KU** and **BCIC-IV-2a**. The best-performing number for each analysis is highlighted in boldface. Method,  $A \rightarrow B$ , is short for the incremental change from baseline A to novel B.

		BCIC-IV-2a $(T \to E)$
Transfer Learning Approach	Acc. Inc.	Acc. Inc.
$MMD \rightarrow RPA$	+2.23%	+3.13%
$DOT(1, 0, 0) \rightarrow (1, 1, 0)$	+1.13%	+0.38%
$DOT(1, 0, 0) \rightarrow (1, 0, 1)$	+2.32%	-0.63%
$DOT(1, 0, 0) \rightarrow (1, 1, 1)$	+1.06%	+2.92%

Particularly, despite the BiMap layer, the internal structure in other layers such as the LOG and fully-connected layers punishes the two losses down to zero. The results exhibit that the proposed approach can minimize the drift of statistical distributions in training.

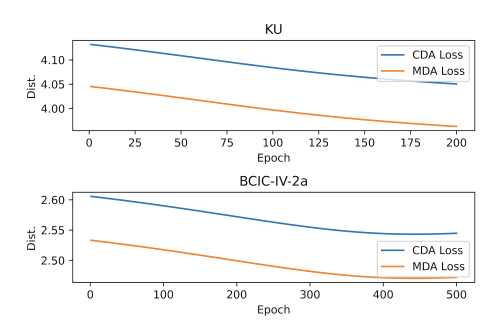


Figure 3: Illustration of average Riemannian distance over epochs on two datasets. Each curve is a sequence of the MDA or CDA loss averages across all the subjects in each dataset during training. The four curves are smooth because we set the size of the whole dataset as the batch size in each iteration.

#### 5.3 Visualization

In this subsection, we plot two-dimensional projections of the outputs of BiMap in DOT using the t-distributed stochastic neighbor embedding (t-SNE) algorithm (Van der Maaten and Hinton, 2008) and visualize the transfer performance of the outputs' marginal and conditional distributions. Since the CE loss enables DOT to trade-off accuracy and transfer performance, we use the loss function without the CE loss, i.e., DOT(0,1,1). For Subject NO.28 in the MI-KU dataset, DOT(1,1,1) achieves accuracy 0.89, whereas DOT(0,1,1) only gets 0.52. Fig. 4 (c) and (d) illustrate projections of outputs of BiMap in DOT(0,1,1) on Subject NO.28 in the KU dataset. In contrast with original datasets, Projection T and Projection V & E shrink together in all four subfigures. We notice that RCT and ROT shrink to a tighter space than the BiMap. Additionally, Fig. 4 (d) exhibits the shrinkage in each class. The above visualization results show that BiMap equipped with the proposed JDA on manifolds is a transfer learning technique (i.e., optimal transport ) linking the source and target domains. For the case of BCIC-IV-2a, we have cautious discussions in Appendix A.

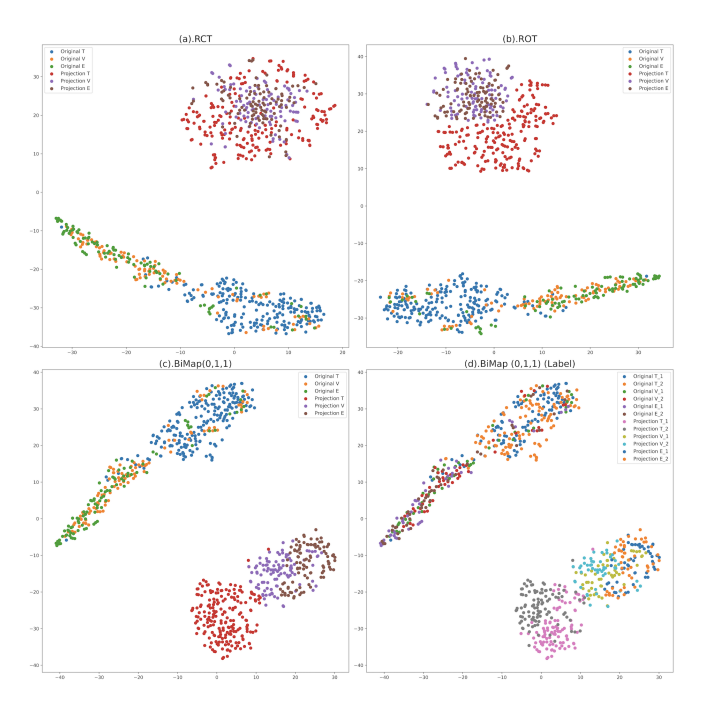


Figure 4: Illustration of 2-dimensional projections on Subject NO.28 of the MI-KU dataset using t-SNE: In each subfigure, we plot point projections of the original dataset and the transformed one after each operation. Fig.(a) and (b) are projections of outcomes after RCT and ROT in RPA; Fig.(c) and (d) are the projections of outputs after the BiMap in DOT(0,1,1), representing the marginal and conditional distributions.

#### 6 DISCUSSIONS

There are two issues that we will have a cautious discussion about in this section. Firstly, DOT is a general machine learning framework applicable to signals and images. We adopt the BCI datasets for verification is because of the highly non-stationarity across sessions proven in neurophysiology (Kaplan *et al.*, 2005). (Refer to Appendix B) Secondly, due to the BCI illiteracy (Thompson, 2019), the improvements of 2.32% and 2.92% on the average accuracy are rather good performance in a cross-session BCI task. Roughly speaking, the condition that the subject using BCI technology fails to reach proficiency in a standard training period is called BCI illiteracy. Lee *et al.* (2019) show that in the MI-KU dataset, the average rates of BCI illiteracy over sessions are over 50%. In other words, it yields that any advanced machine learning technique may fail on at least half of the subjects.

#### 7 CONCLUSIONS

This study proposes a deep network architecture DOT against the DA problem on SPD manifolds using the generalized JDA and the existing architectures of SPDNet. The experiments testify the proposed approach on two highly non-stationary cross-session BCI scenarios. The numerical results exhibit improvements of 2.32% and 2.92% on the two scenarios' average accuracy, respectively. Due to the BCI illiteracy, the improvements are impressive in the domain of BCIs. The visualization results also demonstrate the validity of DOT.

# A Appendix: Visualization of BCIC-IV-2a

In Appendix, to consolidate the arguments in the visualization part, we continue to demonstrate the two-dimensional projections of the other dataset, BICI-IV-2a. Fig. 5 illustrates the original data distribution of two sessions (T and E) from nine subjects in the BCIC-IV-2a dataset, which is computed by the t-distributed stochastic neighbor embedding (t-SNE) algorithm. There is a noticeable drift in the statistical distributions between the T and E sessions for Subject No.2 and NO.5 in Fig. 5. Hence, we plot the two-dimensional projections of the outputs after each operator for Subject 2 and 5 to see if the drift phenomenon disappear or not.

Each subfigure of Fig. 6 contains the projections of the original dataset and the transformed one for a visualized comparison. The projection of original Subject 2 or 5 is the same as the one in Fig. 5 but up to a scale in moving and rotation. The subfigures of RCT and ROT precisely move the source and target domains (T and E) to identity and rotate both domains via parallel transportation. After the rotation, the source and target domains are perfectly separated. For the performance of DOT(0,1,1) on each subfigures (c) and (d) from Subject 2 and 5, we notice that BiMap in DOT(0,1,1) perfectly maps the source and target domains together. Interestingly, each trial in T has a corresponding trial in E with a hardly distinguishable distance, which is probably caused by dataset-specific factors. To sum up, the above-visualized evidence of the projections on the BCIC-IV-2a dataset double demonstrates that BiMap enables DOT, equipped with the generalized JDA on SPD manifolds, to be an optimal transport.

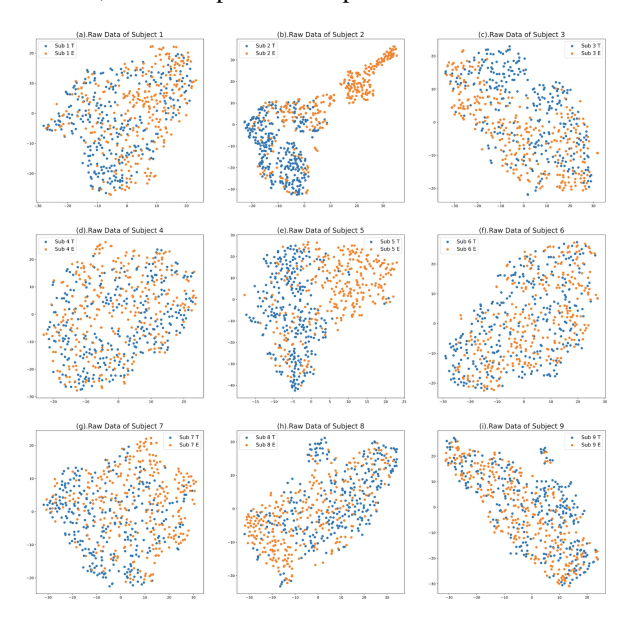


Figure 5: 2-dimensional projection of cross-session scenarios on the BCIC-IV-2a dataset (9 subjects in total) after the t-SNE. For each subject, there are two sessions, i.e. the training (blue) and evaluation (red) sessions, in the BCIC-IV-2a dataset. The time window of the EEG signal is 1000-ms length. There is no overlapping between time windows. Each 2-dimensional color point is dimensionality reduced from a  $9\times20\times20$ -dimensional point, where it has 22 electrodes in the motor cortex region and nine frequency bands.

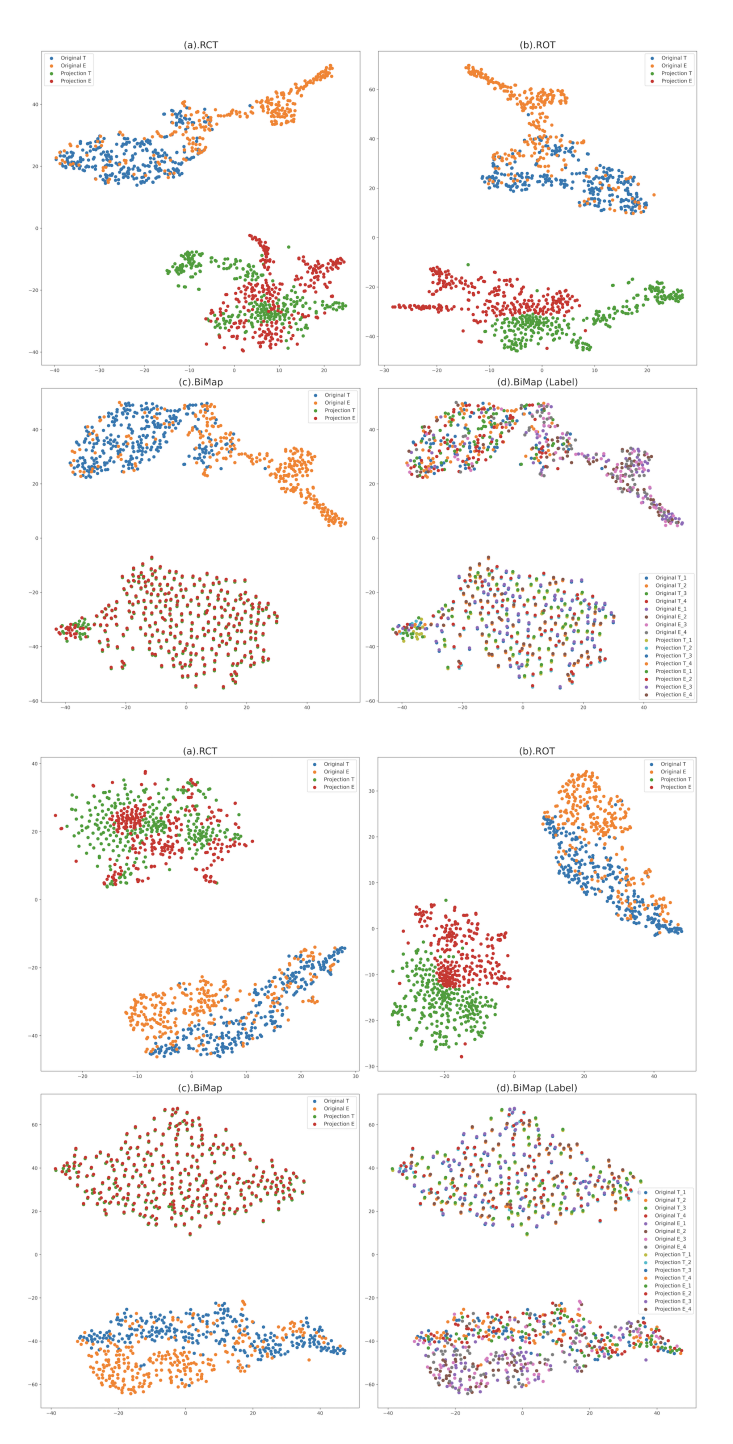


Figure 6: Illustration of 2-dimensional projections on Subject 2 (four top) and 5 (four bottom) of the BCIC-IV-2a dataset after t-SNE. In each subfigure, we plot projections of the original dataset and the transformed one after each operation. Fig.(a) and (b) are projections of outputs after RCT and ROT in RPA; Fig.(c) and (d) are the projections of outputs after the BiMap in DOT(0,1,1), representing the marginal and conditional distributions.

Table 3: Table for several operators on SPD manifolds under the AIRM and LEM metrics.  $D \log$  and  $D \exp$  are the Fréchet derivatives of the principal matrix logarithm  $\log$  and the matrix exponential map  $\exp$  respectively.

	AIRM	LEM
Inner product: $\langle \mathbf{S}_1, \mathbf{S}_2 \rangle_{\mathbf{P}}$	$\operatorname{Tr}\left(\mathbf{P}^{-1}\cdot\mathbf{S}_{1}\cdot\mathbf{P}^{-1}\cdot\mathbf{S}_{2}\right)$	$\langle D \log{(\mathbf{P})}(\mathbf{S}_1), D \log{(\mathbf{P})}(\mathbf{S}_2) \rangle_{\mathbf{I}}$
Riemannian Exponential: $\exp_{\mathbf{P}}(\mathbf{S})$	$\mathbf{P}^{rac{1}{2}}\cdot\exp\left(\mathbf{P}^{-rac{1}{2}}\cdot\mathbf{S}\cdot\mathbf{P}^{-rac{1}{2}} ight)\cdot\mathbf{P}^{rac{1}{2}}$	$\exp(\log(\mathbf{P}) + D\log(\mathbf{P})(\mathbf{S}))$
Riemannian Logarithm: $\log_{\mathbf{P}}(\mathbf{S})$	$\mathbf{P}^{rac{1}{2}} \cdot \log \left( \mathbf{P}^{-rac{1}{2}} \cdot \mathbf{S} \cdot \mathbf{P}^{-rac{1}{2}}  ight) \cdot \mathbf{P}^{rac{1}{2}}$	$D \exp \left(\log \left(\mathbf{P}\right)\right) \left(\log \left(\mathbf{S}\right) - \log \left(\mathbf{P}\right)\right)$
Riemannian Geodesic: $\gamma_t(\mathbf{S}_1,\mathbf{S}_2)$	$\mathbf{S}_{1}^{\frac{1}{2}} \cdot \exp\left(t \cdot \log\left(\mathbf{S}_{1}^{-\frac{1}{2}} \cdot \mathbf{S}_{2} \cdot \mathbf{S}_{1}^{-\frac{1}{2}}\right)\right) \cdot \mathbf{S}_{1}^{\frac{1}{2}}$	$\exp\left(\left(1-t\right)\cdot\log\left(\mathbf{S}_{1}\right)+t\cdot\log\left(\mathbf{S}_{2}\right)\right)$
Riemannian Distance: $\mathcal{L}(\mathbf{S}_1, \mathbf{S}_2)$	$  \log{(\mathbf{S}_{1}^{-rac{1}{2}}\cdot\mathbf{S}_{2}^{rac{1}{2}}\cdot\mathbf{S}_{1}^{-rac{1}{2}})}  _{\mathcal{F}}$	$  \log{(\mathbf{S}_1)} - \log{(\mathbf{S}_2)}  _{\mathcal{F}}$
Weighted Fréchet Mean: $Bar_w(\mathcal{B})$	No Explicit Formula	$\exp\left(\frac{1}{ \mathcal{B} } \cdot \sum_{i} w_i \cdot \log\left(S_i\right)\right)$

# B Appendix: The Nonstationarity Nature of the Brain Activities

In electrophysiological studies, large-scale patterns of synchronized neuronal activity are continually changing over time, and therefore, the signals acquired by the EEG device exhibit considerable variability. For simplicity, the early studies of EEG signals assume the stationarity of signals underlying the data processing and analysis. However, it yields that the essential characteristics of the nonstationarity of EEG signals are almost eliminated. Hence, the new paradigm for analyzing EEG signals is then based on the (essential) nonstationarity of signals that might be caused by switching the inherent metastable states of the neural assemblies during brain functioning. (Kaplan, 1998; Kaplan *et al.*, 2005; Fingelkurts and Fingelkurts, 2004).

For the application scenario in EEG-based BCIs, the nonstationarity nature of the brain activities leads to the variability of EEG signals from calibration to feedback. In recent years, there have been many literatures related to this topic in the BCI community. (Vidaurre et al., 2007; Millán et al., 2007; Blankertz et al., 2007; Von Bünau et al., 2009; Sugiyama et al., 2007; Blumberg et al., 2007; Vidaurre et al., 2010; Shenoy et al., 2006; Li and Guan, 2006; Hasan and Gan, 2009) For instance, Vidaurre et al. (2010) extend the (unsupervised) covariate shift adaptation approach (Shimodaira, 2000; Sugiyama et al., 2007) on BCI scenarios based on a covariate shift assumption that the difference between domains is characterized as a change in the feature space and conditional distributions remain unchanged, i.e.,  $P_S(X_S) \neq P_T(X_T)$ and  $Q_S(Y_S|X_S) = Q_T(Y_T|X_T)$ , improving significantly on several tasks better than the state-of-the-art approaches at that time, and exhibit real examples in which their model is well-fitting on the nonstationarity changes. In this work, the proposed approach does not require such an assumption.

# C Appendix: Riemannian Metrics on SPD manifods

In Section 2.2, we have a brief introduction to  $(S_{++}^n, LEM)$  about its *geodesic* and the Log-Euclidean Fréchet mean. This section will provide a brief discussion on Riemannian metrics on SPD manifolds.

When we talk about a Riemannian manifold, we first need to mention the Riemannian metric. Generally, Riemannian metrics are not unique, and each Riemannian metric defines an as-

sociated distance and other geometric quantities on manifolds. Among many metrics on  $S_{++}^n$ , the most common family of Riemannian metrics are the affine-invariant Riemannian metrics (AIRMs) which has been put forward independently from information science in the 1980s (Burbea and Rao, 1982; Skovgaard, 1984) and many engineering topics (Moakher, 2005; Pennec et al., 2006; Fletcher and Joshi, 2007) around 2005. To illustrate, in diffusion tensor imaging, AIRM is proposed to circumvent the difficulty in the calculations in Euclidean space, for example, a tensor swelling effect Tschumperle and Deriche (2001) that is the determinant of the Euclidean average of SPD matrices can be more significant than one of the original SPD matrices. Formally, AIRMs can be given by one-parameter family up to a global scaling factors as  $\langle V,W\rangle_P=\operatorname{Tr}(VP^{-1}WP^{-1})+\beta\operatorname{Tr}(VP^{-1})\operatorname{Tr}(WP^{-1})$ where  $\beta > -1/n$ . (Pennec, 2006, 2008) All AIRMs yield the same Levi-Civita connection, and therefore, they have the same Riemannian exp and log maps at each point, but the Riemannian distances differ. Meanwhile, the sectional, Ricci, and scalar curvatures on  $(S_{++}^n, AIRM)$  are non-positive. Hence, endowed with AIRM, the SPD manifold becomes a space everywhere non-positive sectional curvature without the cutlocus globally diffeomorphic to the Euclidean space, which is called a Cartan-Hadamard manifold (Li, 2012). There are many nice geometric and statistical properties of SPD manifolds as a Cartan-Hadamard manifold, such as the uniqueness of geodesic joining any two SPD matrices, the existence and uniqueness of the mean of a set of SPD matrices, etc. However, the algorithms on SPD manifolds equipped with AIRM are running slow due to the complex matrix computations. (see Riemannian matrix exponential and logarithm in Table 3.)

To remedy this limitation and overcome the swelling effect simultaneously, another family of Riemannian metrics is the Log-Euclidean metric (LEM) endowed to SPD matrices in this paper. The Log-Euclidean metric also has many excellent properties, including invariance by inversion, logarithmic multiplication, an orthogonal transformation, and scaling. An SPD manifold equipped with LEM is a vector space, and thus it is flat and a Cartan-Hadamard manifold. The most comparative advantage for LEM is to simplify the statistics and analysis on SPD matrices. For instance, Table 3 records the several operators on SPD manifolds under the AIRM and LEM metrics. The weighted Fréchet mean under LEM has an explicit formula, but the affine-invariant one does not have. In the literature Pennec *et al.* (2006), the affine-invariant one is im-

plicitly defined in a barycentric equation and solved iteratively as follows.

$$\mu_{t+1} \leftarrow \mu_t^{\frac{1}{2}} \cdot \exp\left(\frac{1}{|\mathcal{B}|} \cdot \sum_i w_i \cdot \log\left(\mu_t^{-\frac{1}{2}} S_i \mu_t^{-\frac{1}{2}}\right)\right) \cdot \mu_t^{\frac{1}{2}}.$$

The implicit formula is definitely improper to be used in a loss function, and hence, we use LEM to be the Riemannian metric in this paper. For more details on Riemannian metrics on SPD manifolds, an excellent survey of SPD manifolds is dedicated to (Arsigny *et al.*, 2006; Minh and Murino, 2017; Pennec, 2020).

## Acknowledgment

This study is supported under the RIE2020 Industry Alignment Fund–Industry Collaboration Projects (IAF-ICP) Funding Initiative, as well as cash and in-kind contributions from the industry partner(s). This study is also supported by the RIE2020 AME Programmatic Fund, Singapore (No. A20G8b0102).

#### References

- Kai Keng Ang, Zheng Yang Chin, Haihong Zhang, and Cuntai Guan. Filter bank common spatial pattern (fbcsp) in brain-computer interface. In 2008 IEEE international joint conference on neural networks (IEEE world congress on computational intelligence), pages 2390–2397. IEEE, 2008.
- Vincent Arsigny, Pierre Fillard, Xavier Pennec, and Nicholas Ayache. Fast and Simple Computations on Tensors with Log-Euclidean Metrics. PhD thesis, INRIA, 2005.
- Vincent Arsigny, Pierre Fillard, Xavier Pennec, and Nicholas Ayache. Log-euclidean metrics for fast and simple calculus on diffusion tensors. *Magnetic Resonance in Medicine: An Official Journal of the International Society for Magnetic Resonance in Medicine*, 56(2):411–421, 2006.
- Alexandre Barachant, Stéphane Bonnet, Marco Congedo, and Christian Jutten. Multiclass brain–computer interface classification by riemannian geometry. *IEEE Transactions on Biomedical Engineering*, 59(4):920–928, 2011.
- Shai Ben-David, John Blitzer, Koby Crammer, Fernando Pereira, et al. Analysis of representations for domain adaptation. *Advances in neural information processing systems*, 19:137, 2007.
- Rajendra Bhatia. *Positive definite matrices*. Princeton university press, 2009.
- Benjamin Blankertz, Motoaki Kawanabe, Ryota Tomioka, Friederike U Hohlefeld, Vadim V Nikulin, and Klaus-Robert Müller. Invariant common spatial patterns: Alleviating nonstationarities in brain-computer interfacing. In *NIPS*, pages 113–120. Citeseer, 2007.
- Julie Blumberg, Jorn Rickert, Stephan Waldert, Andreas Schulze-Bonhage, Ad Aertsen, and Carsten Mehring. Adaptive classification for brain computer interfaces. In 2007 29th Annual International Conference of the IEEE Engineering in Medicine and Biology Society, pages 2536–2539. IEEE, 2007.
- Daniel Brooks, Olivier Schwander, Frederic Barbaresco, Jean-Yves Schneider, and Matthieu Cord. Riemannian batch normalization for spd neural networks. Advances in Neural Information Processing Systems, 32:15489–15500, 2019.

- Clemens Brunner, Robert Leeb, Gernot Müller-Putz, Alois Schlögl, and GJIFKD Pfurtscheller. Bci competition 2008–graz data set a. *Institute for Knowledge Discovery (Laboratory of Brain-Computer Interfaces), Graz University of Technology*, 16:1–6, 2008.
- Jacob Burbea and C Radhakrishna Rao. Entropy differential metric, distance and divergence measures in probability spaces: A unified approach. *Journal of Multivariate Analysis*, 12(4):575–596, 1982.
- Kai-Xuan Chen, Jie-Yi Ren, Xiao-Jun Wu, and Josef Kittler. Covariance descriptors on a gaussian manifold and their application to image set classification. *Pattern Recognition*, 107:107463, 2020.
- Minhyung Cho and Jaehyung Lee. Riemannian approach to batch normalization. In *Proceedings of the 31st International Conference on Neural Information Processing Systems*, pages 5231–5241, 2017.
- Nicolas Courty, Rémi Flamary, Devis Tuia, and Alain Rakotomamonjy. Optimal transport for domain adaptation. *IEEE transactions on pattern analysis and machine intelligence*, 39(9):1853–1865, 2016.
- Nicolas Courty, Rémi Flamary, Amaury Habrard, and Alain Rakotomamonjy. Joint distribution optimal transportation for domain adaptation. In *Proceedings of the 31st International Conference on Neural Information Processing Systems*, NIPS'17, page 3733–3742, Red Hook, NY, USA, 2017. Curran Associates Inc.
- Andrew A Fingelkurts and Alexander A Fingelkurts. Making complexity simpler: multivariability and metastability in the brain. *International Journal of Neuroscience*, 114(7):843–862, 2004.
- P Thomas Fletcher and Sarang Joshi. Riemannian geometry for the statistical analysis of diffusion tensor data. *Signal Processing*, 87(2):250–262, 2007.
- Bashar Awwad Shiekh Hasan and John Q Gan. Unsupervised adaptive gmm for bci. In 2009 4th International IEEE/EMBS Conference on Neural Engineering, pages 295–298. IEEE, 2009.
- Zhiwu Huang and Luc Van Gool. A riemannian network for spd matrix learning. In *Thirty-First AAAI Conference on Artificial Intelligence*, 2017.
- Jiayuan Huang, Arthur Gretton, Karsten Borgwardt, Bernhard Schölkopf, and Alex Smola. Correcting sample selection bias by unlabeled data. Advances in neural information processing systems, 19:601–608, 2006.
- Ce Ju, Dashan Gao, Ravikiran Mane, Ben Tan, Yang Liu, and Cuntai Guan. Federated transfer learning for eeg signal classification. In 2020 42nd Annual International Conference of the IEEE Engineering in Medicine & Biology Society (EMBC), pages 3040–3045. IEEE, 2020.
- Alexander Ya Kaplan, Andrew A Fingelkurts, Alexander A Fingelkurts, Sergei V Borisov, and Boris S Darkhovsky. Nonstationary nature of the brain activity as revealed by eeg/meg: methodological, practical and conceptual challenges. *Signal processing*, 85(11):2190–2212, 2005.
- A Ia Kaplan. The nonstability of the eeg: a methodological and experimental analysis. *Uspekhi fiziologicheskikh nauk*, 29(3):35–55, 1998.
- Young-Heon Kim and Brendan Pass. Multi-marginal optimal transport on riemannian manifolds. *American Journal of Mathematics*, 137(4):1045–1060, 2015.
- Zoltan J Koles, Michael S Lazar, and Steven Z Zhou. Spatial patterns underlying population differences in the background eeg. *Brain topography*, 2(4):275–284, 1990.

- Soheil Kolouri, Se Rim Park, Matthew Thorpe, Dejan Slepcev, and Gustavo K Rohde. Optimal mass transport: Signal processing and machine-learning applications. *IEEE signal processing magazine*, 34(4):43–59, 2017.
- Vernon J Lawhern, Amelia J Solon, Nicholas R Waytowich, Stephen M Gordon, Chou P Hung, and Brent J Lance. Eegnet: a compact convolutional neural network for eeg-based brain– computer interfaces. *Journal of neural engineering*, 15(5):056013, 2018.
- Min-Ho Lee, O-Yeon Kwon, Yong-Jeong Kim, Hong-Kyung Kim, Young-Eun Lee, John Williamson, Siamac Fazli, and Seong-Whan Lee. Eeg dataset and openbmi toolbox for three bci paradigms: an investigation into bci illiteracy. *GigaScience*, 8(5):giz002, 2019.
- Yuanqing Li and Cuntai Guan. An extended em algorithm for joint feature extraction and classification in brain-computer interfaces. *Neural computation*, 18(11):2730–2761, 2006.
- Yan Li, Hiroyuki Kambara, Yasuharu Koike, and Masashi Sugiyama. Application of covariate shift adaptation techniques in brain-computer interfaces. *IEEE Transactions on Biomedical Engineering*, 57(6):1318–1324, 2010.
- Peter Li. *Geometric analysis*, volume 134. Cambridge University Press, 2012.
- Mingsheng Long, Jianmin Wang, Guiguang Ding, Jiaguang Sun, and Philip S Yu. Transfer feature learning with joint distribution adaptation. In *Proceedings of the IEEE international conference on computer vision*, pages 2200–2207, 2013.
- Robert J McCann. Polar factorization of maps on riemannian manifolds. Geometric & Functional Analysis GAFA, 11(3):589–608, 2001.
- José del R Millán, Anna Buttfield, Carmen Vidaurre, Rafael Cabeza, Alois Schlögl, Gert Pfurtscheller, Pradeep Shenoy, and Rajesh PN Rao. 18 adaptation in brain-computer interfaces. *Toward Brain-Computer Interfacing*, page 303, 2007.
- Hà Quang Minh and Vittorio Murino. Covariances in computer vision and machine learning. Synthesis Lectures on Computer Vision, 7(4):1–170, 2017.
- Maher Moakher. A differential geometric approach to the geometric mean of symmetric positive-definite matrices. *SIAM Journal on Matrix Analysis and Applications*, 26(3):735–747, 2005.
- Xavier Pennec, Pierre Fillard, and Nicholas Ayache. A riemannian framework for tensor computing. *International Journal of com*puter vision, 66(1):41–66, 2006.
- Xavier Pennec. Statistical computing on manifolds for computational anatomy. PhD thesis, Université Nice Sophia Antipolis, 2006.
- Xavier Pennec. Statistical computing on manifolds: from riemannian geometry to computational anatomy. In LIX Fall Colloquium on Emerging Trends in Visual Computing, pages 347–386. Springer, 2008.
- Xavier Pennec. Manifold-valued image processing with spd matrices. In *Riemannian geometric statistics in medical image analysis*, pages 75–134. Elsevier, 2020.
- Peter Petersen, S Axler, and KA Ribet. *Riemannian geometry*, volume 171. Springer, 2006.
- Pedro Luiz Coelho Rodrigues, Christian Jutten, and Marco Congedo. Riemannian procrustes analysis: transfer learning for braincomputer interfaces. *IEEE Transactions on Biomedical Engineering*, 66(8):2390–2401, 2018.

- Robin Tibor Schirrmeister, Jost Tobias Springenberg, Lukas Dominique Josef Fiederer, Martin Glasstetter, Katharina Eggensperger, Michael Tangermann, Frank Hutter, Wolfram Burgard, and Tonio Ball. Deep learning with convolutional neural networks for eeg decoding and visualization. *Human brain mapping*, 38(11):5391–5420, 2017.
- Pradeep Shenoy, Matthias Krauledat, Benjamin Blankertz, Rajesh PN Rao, and Klaus-Robert Müller. Towards adaptive classification for bci. *Journal of neural engineering*, 3(1):R13, 2006.
- Hidetoshi Shimodaira. Improving predictive inference under covariate shift by weighting the log-likelihood function. *Journal of statistical planning and inference*, 90(2):227–244, 2000.
- Lene Theil Skovgaard. A riemannian geometry of the multivariate normal model. Scandinavian journal of statistics, pages 211–223, 1984
- Masashi Sugiyama, Matthias Krauledat, and Klaus-Robert Müller. Covariate shift adaptation by importance weighted cross validation. *Journal of Machine Learning Research*, 8(5), 2007.
- Baochen Sun and Kate Saenko. Deep coral: Correlation alignment for deep domain adaptation. In *European conference on computer vision*, pages 443–450. Springer, 2016.
- Baochen Sun, Jiashi Feng, and Kate Saenko. Correlation alignment for unsupervised domain adaptation. In *Domain Adaptation in Computer Vision Applications*, pages 153–171. Springer, 2017.
- Margaret C Thompson. Critiquing the concept of bci illiteracy. *Science and engineering ethics*, 25(4):1217–1233, 2019.
- David Tschumperle and Rachid Deriche. Diffusion tensor regularization with constraints preservation. In *Proceedings of the 2001 IEEE Computer Society Conference on Computer Vision and Pattern Recognition. CVPR 2001*, volume 1, pages I–I. IEEE, 2001.
- Laurens Van der Maaten and Geoffrey Hinton. Visualizing data using t-sne. *Journal of machine learning research*, 9(11), 2008.
- Carmen Vidaurre, A Schlogl, Rafael Cabeza, Reinhold Scherer, and Gert Pfurtscheller. Study of on-line adaptive discriminant analysis for eeg-based brain computer interfaces. *IEEE transactions on biomedical engineering*, 54(3):550–556, 2007.
- Carmen Vidaurre, Motoaki Kawanabe, Paul von Bünau, Benjamin Blankertz, and Klaus-Robert Müller. Toward unsupervised adaptation of lda for brain-computer interfaces. *IEEE Transactions on Biomedical Engineering*, 58(3):587–597, 2010.
- Cédric Villani. *Optimal transport: old and new*, volume 338. Springer, 2009.
- Paul Von Bünau, Frank C Meinecke, Franz C Király, and Klaus-Robert Müller. Finding stationary subspaces in multivariate time series. *Physical review letters*, 103(21):214101, 2009.
- Or Yair, Felix Dietrich, Ronen Talmon, and Ioannis G Kevrekidis. Domain adaptation with optimal transport on the manifold of spd matrices. *arXiv* preprint arXiv:1906.00616, 2019.